

DYNAMICS OF STARS AND GLOBULAR CLUSTERS IN M87

Aaron J. Romanowsky

Kapteyn Astronomical Institute, P.O. Box 800, 9700 AV Groningen, The Netherlands
 and Harvard-Smithsonian Center for Astrophysics, 60 Garden Street, Cambridge MA 02138
 Email: romanow@astro.rug.nl

Christopher S. Kochanek

Harvard-Smithsonian Center for Astrophysics, MS-51, 60 Garden Street, Cambridge MA 02138
 Email: ckochanek@cfa.harvard.edu

ABSTRACT

We examine the dynamics of the stars and globular clusters in the nearby giant galaxy M87 and constrain the mass distribution, using all the available data over a large range of radii, including higher-order moments of the stellar line-of-sight velocity distributions and the discrete velocities of over two hundred globular clusters. We introduce an extension of the spherical orbit modeling method that makes full use of all the information in the data, and provides very robust constraints on the mass models. We conclusively rule out a constant mass-to-light ratio model. Using the stellar constraints, the mass of the dark halo is determined to 9% accuracy, assuming a singular isothermal density profile. The globular cluster constraints determine the mass to 14%. However, the masses that we infer separately with these constraints are inconsistent. This implies that the halo's radial density profile falls off more slowly than r^{-2} , suggesting that the potential of the Virgo Cluster is already dominant at $r \sim 300'' \sim 20$ kpc.

Subject headings: galaxies: elliptical and lenticular, cD — galaxies: halos — galaxies: individual (M87) — galaxies: kinematics and dynamics — galaxies: star clusters — galaxies: structure — globular clusters: general

1. INTRODUCTION

Elliptical galaxies lack the dynamical simplicity of spiral galaxies, posing well-known challenges for determining their intrinsic properties (*e.g.*, mass distribution, shape, orbit structure). The projected stellar velocity dispersion radial profile, $\hat{\sigma}_p(R)$, is easily measured, but is subject to a degeneracy between the mass distribution and the orbital anisotropy, where radial variations in the stellar orbit types mask or mimic changes in the mass-to-light ratio (M/L) (Binney & Mamon 1982; Tonry 1983). Crucial for resolving this degeneracy is the measurement of higher-order moments of

the stellar line-of-sight velocity distributions (LOSVDs). Such LOSVD information has been used to constrain the masses of central Black holes (van der Marel *et al.* 1998; Emsellem, Dejonghe, & Bacon 1999; Gebhardt *et al.* 2000) and dark halos (Carollo *et al.* 1995; Rix *et al.* 1997; Gerhard *et al.* 1998). Unfortunately, the surface brightness of an elliptical declines rapidly with radius, making these measurements increasingly difficult at the large radii where the dark matter problem becomes most interesting ($\gtrsim 2 R_{\text{eff}}$). Other techniques are necessary to probe this outer mass distribution.

In nearby galaxies, the two main candidates for such probes are X-ray emission from extended hot gas (see Fabbiano 1989 §4.4 for a review), and the discrete velocities of either planetary nebulae (*e.g.*, Ciardullo, Jacoby, & Dejonghe 1993; Tremblay, Merritt, & Williams 1995; Hui *et al.* 1995; Arnaboldi *et al.* 1998) or globular clusters (*e.g.*, Cohen & Ryzhov 1997, hereafter CR; Sharples *et al.* 1998; Kissler-Patig *et al.* 1999). However, the analysis of discrete kinematical measurements calls for more refined dynamical models than either simple virial estimators (*e.g.*, Heisler, Tremaine, & Bahcall 1985; Kent 1990; Haller & Melia 1996) or binning the data and using the Jeans equations (*e.g.*, Federici *et al.* 1993; Grillmair *et al.* 1994; Tremblay *et al.* 1995). These procedures do not guarantee a physical solution, make unwarranted assumptions about the orbital anisotropy, and do not make full use of the constraints provided by the data. The first two deficiencies are alleviated by techniques employing distribution function (DF) basis sets that permit the full freedom of orbit types (*e.g.*, Merritt, Meylan, & Mayor 1997; Mathieu & Dejonghe 1999; Saglia *et al.* 2000). But these techniques typically bin the data in radius and velocity, destroying potentially useful information, such as the maximum observed velocity as a direct constraint on the escape velocity. More general methods are needed to make better use of the information contained in the discrete velocity data; Merritt & Saha (1993) and Merritt (1993) have demonstrated one such approach using DF basis sets and maximum likelihood methods. We develop a general dynamical method based on orbit modeling, and apply it to a real galaxy, M87.

The giant central Virgo Cluster galaxy M87 (= NGC 4486), although not a typical elliptical, is nevertheless a prime candidate for modeling because of the abundance of data available on it. In addition to high-precision measurements of its higher-order stellar velocity moments and of the radially-extended velocity dispersion, it has the largest available sample of globular cluster (GC) velocity measurements. The stellar velocity measurements extend out to $\sim 1.5 R_{\text{eff}}$, and the GC measurements to $\sim 5 R_{\text{eff}}$, probing well into the area where the dynamics are presumably dominated by the dark halo of the galaxy or the Virgo Cluster. The combination of these kinematical constraints should provide robust limits on the dark matter distribution, and on the orbital structures of both the stars and the GCs.

While a variety of modeling techniques have been used to study the stellar dynamics of M87 (Sargent *et al.* 1978; Duncan & Wheeler 1980; Binney & Mamon 1982; Newton & Binney 1984; Richstone & Tremaine 1985; Dressler & Richstone 1990; Tenjes, Einasto, & Haud 1991; van der Marel 1994; Merritt & Oh 1997), they concentrated on its central regions in order to constrain the mass of a central black hole. The stellar dynamics of its *halo* have not been modeled in detail, nor have the higher-order velocity moments been used as strict constraints. But the best available

tracers of the halo mass distribution are ultimately the GCs and the hot gas, which can be easily observed at large radii. Some simple dynamical methods have been used to estimate the halo mass using the GCs (Merritt & Tremblay 1993; CR). They claim that the radially-rising velocity dispersion profile rules out a constant M/L model, and that it suggests that the GCs are in fact tracing the Virgo Cluster potential rather than M87’s own potential (as suggested also by analyses of the X-ray emission and the kinematics of the cluster galaxies; *e.g.*, see Nulsen & Böhringer 1995; McLaughlin 1999). But a more rigorous dynamical model, allowing for all the systematic orbital uncertainties, is necessary to confirm these findings. We will apply our general orbit modeling method, using a large sample (~ 200) of discrete GC velocities, to see how the GCs — alone and jointly with the stellar dynamics — constrain two simple limiting models of the mass distribution. In §2 we detail the observational constraints for M87. We describe our modeling methods in §3, §4 presents the results, and the conclusions are in §5.

2. OBSERVATIONAL CONSTRAINTS

Here we summarize the observational constraints on M87. These include the stellar surface brightness (§2.1); velocity measurements of the stars (§2.2); the globular cluster surface density (§2.3); and globular cluster discrete velocity measurements (§2.4). We assume a distance to M87 of 15 Mpc (Pierce *et al.* 1994), so that $1'' = 73$ pc and $1' = 4.4$ kpc. The stellar effective radius is $R_{\text{eff}} \simeq 100''$ (Burstein *et al.* 1987; Zeilinger, Møller, & Stiavelli 1993).

2.1. Stellar Surface Brightness

For the stellar surface brightness radial profile $\mu(R)$ in the core region ($R=0''.01$ – $8''$) we use the *HST I*-band data of Lauer *et al.* (1992). We use their seeing-deconvolved profile, and approximate the photometric uncertainties by $\Delta\mu = \max[0''.011/R, 0.02]$. For the outer regions ($R=8''$ – $745''$), we use the *B*-band data of Capaccioli, Caon, & Rampazzo (1990), with the photometric uncertainties estimated from their Figure 3, and with an offset of 2.78 magnitudes to match the profile to the Lauer *et al.* (1992) data. The color gradients are quite small over the entire range of the galaxy ($|\Delta(B - I)|_{\text{max}} < 0.2$ mag; *e.g.*, Boroson *et al.* 1983; Cohen 1986; Zeilinger *et al.* 1993), so there should be little systematic problem in combining the *I*-band and *B*-band data. The isophote ellipticity varies from 0.02 at $2''$ to 0.1 at $75''$ to 0.35 at $500''$. The dynamics of the galaxy depend on the ellipticity of its gravitational potential, which is much rounder than its density distribution ($\epsilon_\Phi \sim \epsilon_\rho/3$; Binney & Tremaine 1987 §2.3.1), so it will be a reasonable approximation to treat the galaxy as spherical. We map all the data from the major axis a to the intermediate axis $m = a\sqrt{1 - \epsilon}$.

For the purposes of our mass modeling, we project and fit a parameterized luminosity density model to the data of the form $\nu(r) \propto r^{-\alpha_1}(r^3 + s_1^3)^{-\alpha_2}(r + s_2)^{-\alpha_3}$, and find $\alpha_1 = 1.22$, $\alpha_2 = 0.361$,

$\alpha_3 = 1.26$, $s_1 = 9.^{\circ}38$, and $s_2 = 170''$, with a χ^2 statistic for the fit of 35.1 for 142 degrees of freedom. This functional fit will only be used to generate a constant M/L gravitational potential, while we will directly fit the surface brightness data in our dynamical models (§3). Note that in M87, $\mu(R)$ does not taper off steeply in the outer regions as in normal $R^{1/4}$ ellipticals — a typical R^{-2} cD envelope (Schombert 1986) begins at $R \gtrsim 300''$. An old dispute over the brightness of this envelope (see *e.g.*, de Vaucouleurs & Nieto 1978; Carter & Dixon 1978) has not been resolved, presumably because of sky-subtraction problems for such a large, low-surface-brightness structure. Our asymptotic radial slope lies between the reported extremes.

2.2. Stellar Velocities

For the core region ($R < 29''$), we use the G -band data from van der Marel (1994, hereafter vdM) for the projected stellar velocity dispersion $\hat{\sigma}_p(R)$ and the Gauss-Hermite velocity moments $h_4(R)$ and $h_6(R)$ (see §3). For the outer regions ($R=28''$ – $168''$), we use $\hat{\sigma}_p(R)$ from Sembach & Tonry (1996, hereafter ST). We combine the data from positive and negative radii into one radial profile. There appears to be a systematic velocity offset between the ST data and most other data (Sargent *et al.* 1978; Davies & Birkinshaw 1988; Jarvis & Peletier 1991; Winsall & Freeman 1993), presumably due to the large slit width; we estimate that this corresponds to an additional instrumental dispersion of $183 \pm 11 \text{ km s}^{-1}$, which we remove from the ST data in order to match them to the vdM data. The final velocity dispersion profile is nearly constant for $R < 1''$, outside of which it falls off slowly with radius ($\hat{\sigma}_p \sim R^{-0.1}$). Comparing h_4 and h_6 from positive and negative radii, we find differences larger than are consistent with the stated uncertainties. We assume the errors were underestimated by 12% and 22% to bring the profiles into statistical agreement. The departures from Gaussianity of the LOSVD are everywhere small (typically, $|h_4|, |h_6| < 0.02$).

2.3. Globular Cluster Surface Density

Our GC surface density radial profile $N(R)$ is taken from the number counts of Kundu *et al.* (1999) for $R = 0''$ – $96''$ (with their quoted uncertainties). For $R = 84''$ – $472''$, we take the data from McLaughlin, Harris, & Hanes (1993), adding in their 0.4 arcmin^{-2} background uncertainty, and multiplying by 1.45 to match the normalization of the Kundu *et al.* (1999) data. For $R = 419''$ – $1351''$, we use the data from Harris (1986) after subtracting their background count of $5.8 \pm 0.3 \text{ arcmin}^{-2}$ and normalizing by a factor of 2.19. We do not convert any of these profiles to an intermediate axis since this is already effectively accomplished by the derivation method (counting in circular annuli). Like the stellar surface brightness, the GC surface density decreases slowly with radius in the central regions ($\sim R^{-0.3}$), and changes over to a steeper power law in the outer parts ($\sim R^{-1.6}$); however, the radius where this break occurs is much larger for the GCs ($R_b \sim 60''$ vs. $10''$), indicating that these systems are dynamically distinct.

2.4. Globular Cluster Discrete Velocities

For the GC line-of-sight velocities v_z , we use data from Mould, Oke, & Nemec (1987), Huchra & Brodie (1987), Mould *et al.* (1990), CR, and Cohen (2000). Most of the positions are taken from Strom *et al.* (1981). We compare the velocities of common objects to determine the systematic offset between the data sets, and to estimate the measurement uncertainties ($\Delta v_z \sim 100 \text{ km s}^{-1}$). We discard as foreground stars all objects with heliocentric velocities $v_z < 250 \text{ km s}^{-1}$, and as background galaxies all those with $v_z > 2650 \text{ km s}^{-1}$. We examine the colors and magnitudes of objects with $v_z < 500 \text{ km s}^{-1}$ to distinguish GCs from stars. Objects of uncertain identification are discarded. We map the data to the intermediate axis m , using ellipticity estimates from McLaughlin, Harris, & Hanes (1994). Our final data set has 234 velocities from $R = 25''$ – $526''$ (see Fig. 1).

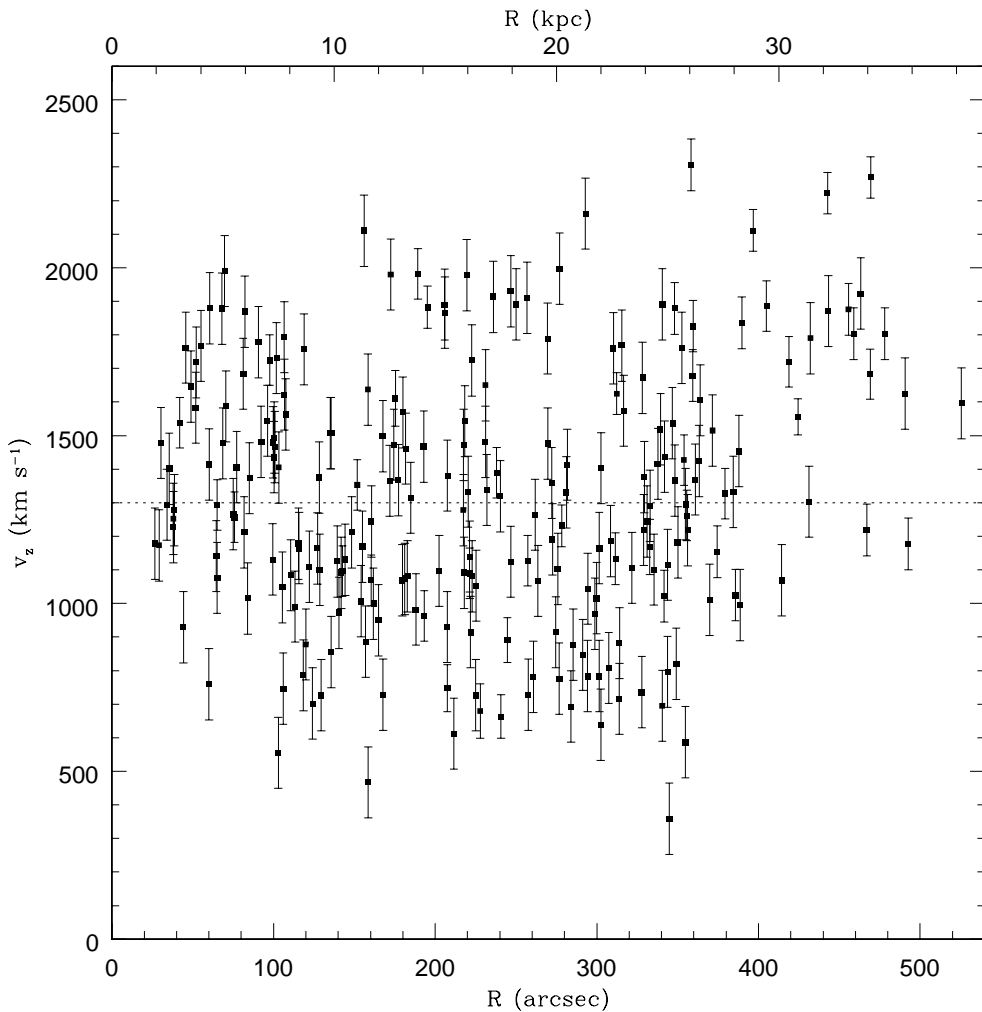


FIG. 1.— Line-of-sight velocities for 234 globular clusters around M87, as a function of galactocentric radius R . The dotted line shows a systemic velocity of 1300 km s^{-1} .

There is a paucity of low velocity measurements at large radii, which may be related to the rotation of the GCs along the galaxy’s major axis in the outer parts, as demonstrated by Kissler-Patig & Gebhardt (1998). For the GCs with $R \geq 370''$, there were only 4 measurements taken on the “approaching” side and 23 on the “receding” side. Thus, the large-radius velocity asymmetry is probably due to incomplete spatial coverage, which may make our mean velocity for the system systematically high (it is decreased from 1352 to 1293 km s^{-1} if the clusters with $R \geq 370''$ are omitted). This is also suggested by the global velocity distribution (Fig. 2), which appears more symmetric if the mean velocity is set to ~ 1300 km s^{-1} . The best-fit Gaussian curve to the data has a central velocity of $\hat{v}_p = 1323 \pm 28$ km s^{-1} (1308 ± 29 km s^{-1} if the outer clusters are omitted). We adopt a systemic velocity of 1300 km s^{-1} , which we subtract from the measurements to get the galactocentric velocities. This compares well with estimates of the stellar mean redshift from vdM (1277 km s^{-1}), ST (1293 km s^{-1}), and the RC3 (1282 ± 9 km s^{-1} ; de Vaucouleurs *et al.* 1991). The large-radius velocity asymmetry will not pose any further difficulties because we will model only the *even* part of the DF, so that all the discrete velocities are implicitly considered as present also at their reflected position about the mean velocity.

Fig. 2 also suggests that the GCs have a tangentially-biased orbit distribution, which typically produces a flat or double-peaked LOSVD. We fit a fourth-order Gauss-Hermite velocity moment (see §3) to the system, finding $h_4 = -0.04 \pm 0.02$ ($\hat{\sigma}_p = 404 \pm 16$ km s^{-1}), which is weakly suggestive of tangential anisotropy. A double-peaked LOSVD (especially evident at larger radii) has also been found in the GC system of the Fornax Cluster cD galaxy NGC 1399 (Kissler-Patig *et al.* 1999).

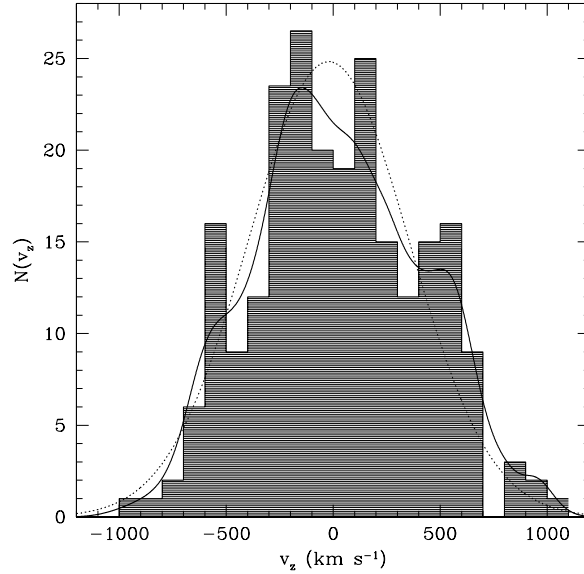


FIG. 2.— Distribution of globular cluster line-of-sight velocities, relative to a systemic velocity of 1300 km s^{-1} . The histogram shows the number of data points in velocity bins. The solid curve shows a smoothed superposition of the measurements. The dotted curve shows the best-fit Gaussian curve to the data ($\sigma = 376$ km s^{-1}). Note the double peaks of low significance at ± 200 km s^{-1} and at ± 500 km s^{-1} .

3. METHODS

The method of orbit modeling was pioneered by Schwarzschild (1979) to reproduce the observed density distribution of a galaxy from a weighted library of representative particle orbits. Given a fixed gravitational potential $\Phi(r)$, the solutions are nonparametric — no functional form is assumed for the DF — so that one need not worry that the models cannot fully explore the possible solutions. The DF is guaranteed to be nonnegative and physical. This method was extended by Richstone & Tremaine (1984) to include projected velocity dispersion information, and by Rix *et al.* (1997) to include higher-order velocity moments. We used similar techniques to examine the uncertainty in a high-redshift galaxy’s mass as implied by a measurement of its central velocity dispersion — an important step in determining H_0 from certain gravitational lens systems (Romanowsky & Kochanek 1999, hereafter Paper I). Other recent orbit modeling efforts have concentrated on applying the method to three-integral axisymmetric systems (*e.g.*, van der Marel *et al.* 1998; Gebhardt *et al.* 2000). Here we extend our spherical method to include the discrete velocities of GCs. The outline of the method is as follows.

We begin with an assumed radial profile for the mass density distribution $\rho(r)$. Our first model is a simple representation of a dark-matter dominated system, the singular isothermal sphere (SIS): $\rho(r) = \sigma_0^2/2\pi Gr^2$. The second model is the constant M/L distribution described in §2.1, parameterized by Υ_B : the ratio of the mass density $\rho(r)$ and the B -band luminosity density $\nu(r)$, with units of $M_\odot/L_{B\odot}$. We pick a random distribution of orbits that densely samples the phase space of energy and angular momentum $(E, |L|)$. The initial radii r_{0k} of the orbits are logarithmically spaced in r_0 , and the energy E_k of each orbit is selected to correspond to that of a circular orbit at this radius, $\Phi(r_{0k}) + v_c^2(r_{0k})/2$. For the SIS model, this procedure produces a sampling that is uniform in energy. The angular momentum L_k of the orbit is selected randomly from the range $[0, L_{\max,k}]$, where $L_{\max,k} = r_{0k}v_c(r_{0k})$. For both the stellar models and the GC models, we use 2500 particle orbits. For the stars, r_0 spans the range $0''\text{--}4450''$, resulting in a radial coverage of $r = 0''\text{--}7330''$ (SIS model) or $r = 0''\text{--}8710''$ (constant M/L model). For the GCs, $r_0 = 10''\text{--}13360''$, corresponding to $r = 0''\text{--}22030''$ (SIS model) or $r = 0''\text{--}26420''$ (constant M/L model).

We next compute the orbit projection “kernels”, which correspond to the contribution of each orbit to each observable. The predictions of the model can then be expressed as follows:

$$y_i^m = \sum_k w_k^2 \langle K_{ik} \rangle_{t,\theta,\phi}, \quad (1)$$

where the \mathbf{w} are the orbit weights, and the kernels \mathbf{K} have been averaged over time and over all spherical-polar viewing angles (θ, ϕ) . For example, the kernel for the angle-averaged surface density in an annulus between R_1 and R_2 of an orbit at an instantaneous radius r' is given by the integral

$$\langle K_{I(R_1,R_2)} \rangle_{\theta,\phi}(r') = \frac{1}{\pi(R_2^2 - R_1^2)} \int_{R_1}^{R_2} 2\pi R dR \int_R^\infty \frac{\delta(r - r')}{4\pi r^2} \frac{2r dr}{\sqrt{r^2 - R^2}} \int_0^{2\pi} \frac{d\xi}{2\pi} \quad (2)$$

$$= \frac{\sqrt{1 - R_1^2/r'^2} - \sqrt{1 - R_2^2/r'^2}}{\pi(R_2^2 - R_1^2)}, \quad (3)$$

where the orbit’s instantaneous density is $\delta(r - r')/4\pi r^2$, the variable ξ represents the line of sight’s position in the tangential plane (θ, ϕ) , and the integration is carried out along the line of sight $z = \pm\sqrt{r^2 - R^2}$. The viewing-angle integral (along $d\xi$) is nontrivial for kernels that involve velocity measurements. Placed at the initial radius r_0 , the orbit is run forward in time for one radial period T_r , and the final kernel is found by averaging over time:

$$\langle K \rangle_{t,\theta,\phi} = \frac{1}{T_r} \int_0^{T_r} \langle K \rangle_{\theta,\phi}(t) dt,$$

where the integration is handled by a Bulirsch-Stoer type integrator.

We must calculate the model’s LOSVD, $dL/dv_p(v_p, R)$, to fit the observed stellar velocity moments $(\hat{\sigma}_p, h_4, h_6)$ and the GC velocity measurements. The LOSVD kernels $K_{dL/dv_p(R),k}$ for a measurement at radius R are binned in velocity with $v_p = [0..v_{\max}]$, where $v_{\max}(R)$ is the velocity of a particle at radius $r = R$ that has plunged inward on a radial orbit from the largest possible radius. For the constant M/L model, this implies that $v_{\max} \simeq v_{\text{esc}}$ (the escape velocity). Our models are symmetric in velocity, *i.e.*, $dL/dv_p(v_p) = dL/dv_p(-v_p)$. By construction, v_{\max}^2 scales linearly with the mass normalization of the galaxy model (σ_0^2 or Υ_B), so that we can use the same binned LOSVD kernels when changing the mass scale.

The Gauss-Hermite velocity moments h_l , which measure deviations of a LOSVD from a Gaussian, are defined by

$$h_l \equiv \frac{\sqrt{2}\gamma_0}{\hat{\gamma}_p} \int_{-\infty}^{\infty} \frac{dL}{dv_p}(v_p) e^{-\hat{w}^2/2} H_l(\hat{w}) dv_p, \quad (4)$$

where $\hat{w} = (v_p - \hat{v}_p)/\hat{\sigma}_p$, γ_0 is the line strength, $(\hat{\gamma}_p, \hat{v}_p, \hat{\sigma}_p)$ are the coefficients for the best Gaussian fit to dL/dv_p , and $H_l(\hat{w})$ are the Hermite polynomials (van der Marel & Franx 1993). The moments (h_4, h_6) measure how flat ($h_4 < 0, h_6 > 0$) or how peaked ($h_4 > 0, h_6 < 0$) the LOSVD is compared to a Gaussian, where these signatures are typically produced by tangential and radial orbits, respectively. The two moments differ in how much weight they put in the high-velocity wings of the LOSVD. In Paper I, we fitted a Gaussian curve to the LOSVD to find $(\hat{\gamma}, \hat{\sigma}_p)$ at each step in our minimization routine, and then calculated h_4 ; this is equivalent to solving the nonlinear equations $h_0 = 1$ and $h_2 = 0$. Here, we expand the Gauss-Hermite series about the fixed data values $\hat{\sigma}_p^d$. Rather than directly fitting $\hat{\sigma}_p^d$, we equivalently fit the second-order moment $h_2 = 0.00 \pm \Delta h_2$, where $\Delta h_2 \simeq \Delta \hat{\sigma}_p / \sqrt{2} \hat{\sigma}_p^d$. With this formulation, calculating the model’s velocity observables is now linear with respect to the orbit weights. We use 41 velocity bins from $v_p = 0$ to v_{\max} to numerically integrate equation (4), which we have heuristically found to give very good accuracy. Note that because our model is completely spherically symmetric (simulating only the even part of the DF), it would be more appropriate to fit measurements of z_4 (expanded around $\hat{v}_p = 0$) rather than h_4 (see van der Marel *et al.* 1994 §5.1); however, these measurements are not available for M87. Since the measured rotation is small ($\sim 10 \text{ km s}^{-1}$), the difference would be unimportant.

The kernels $(\mathbf{K}_I, \mathbf{K}_{dL/dv_p})$ need be computed only once for each galaxy mass model. We then adjust the weights of the orbits so that the model’s projected observables \mathbf{y}^m (equation 1) best

fit the data \mathbf{y}^d . For most of the data $(I, \hat{\sigma}_p, h_4, h_6)$, we express the likelihood of the fit using the standard χ^2 statistic,

$$\chi^2 = \sum_i \left(\frac{y_i^m - y_i^d}{\sigma_i} \right)^2, \quad (5)$$

where the measurement uncertainty is σ_i , while the likelihood function for the discrete velocities and positions of the GCs is

$$\mathcal{L}_i(v_i, R_i) \propto \int \frac{dL}{dv_p}(v_p, R_i) e^{-(v_i - v_p)^2 / 2\sigma_i^2} dv_p, \quad (6)$$

where $v_i \pm \sigma_i$ are the individual velocity measurements. In maximizing \mathcal{L}_i , we are forcing the LOSVD to peak at the measured velocities v_i weighted by the measurement errors σ_i . This is schematically illustrated in Fig. 3. Given complete freedom, this method would produce a best-fit solution whose LOSVDs resembled δ -functions at the measurements v_i . However, the model's averaging in angle and time produces an intrinsic smoothing to the LOSVDs, and does not permit such unphysical solutions. For the current implementation, we use 15 velocity bins from $v_p = 0$ to v_{\max} for the LOSVD at each radius in order to compute the integral in equation (6). Note that our method does not require binning the velocities in radius, nor computing velocity moments.

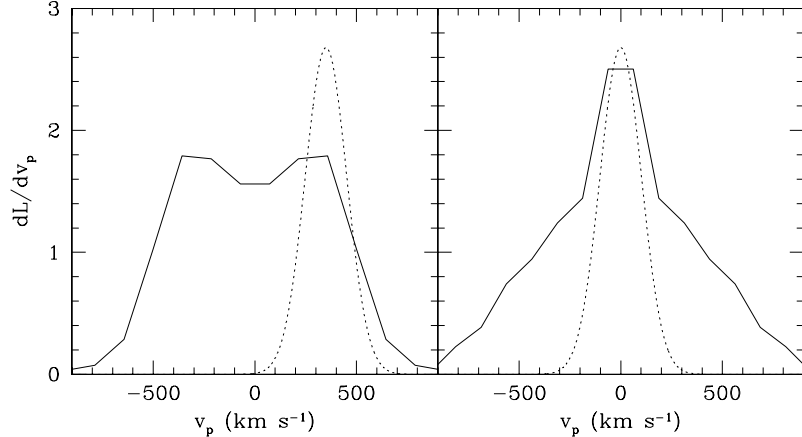


FIG. 3.— Schematic line-of-sight velocity distributions (*solid curves*), fitted to discrete velocity data (*dotted curves*). The double-peaked LOSVD on the left is indicative of tangential anisotropy, while the centrally-peaked LOSVD on the right indicates radial anisotropy.

The final function which we will minimize is

$$f(\mathbf{w}) \equiv \frac{1}{2} \chi^2 - \sum_i \ln \mathcal{L}_i + \lambda S, \quad (7)$$

where S is a measure of entropy:

$$S = \sum_k w_k^2 \ln w_k^2. \quad (8)$$

We employ this smoothing function S as a heuristic device for quickly reaching a rough solution; in our final solutions, the Lagrangian factor λ is reduced to such a low value ($\sim 10^{-5}$) so as to make the entropy constraints inconsequential. With no such regularization imposed, this is an ill-conditioned inversion problem, so our DF solutions will be choppy in a way that real galaxies' DFs presumably are not. However, our methods are the statistically correct way to handle the uncertainties, absent any other *a priori* smoothness conditions. We use a conjugate gradient method (see Press *et al.* 1992 §10.6) with first and second derivative information, to minimize f . We have tested our methods on an isotropic Hernquist (1990) model to demonstrate that we recover correctly the input mass, given constraints on $I(R)$ and $\hat{\sigma}_p(R)$ (see Paper I).

4. RESULTS

We first fit the two mass models (SIS and constant M/L) to the stellar data [$I(R)$, $\hat{\sigma}_p(R)$, $h_4(R)$, $h_6(R)$] over a sequence of the mass parameters σ_0 and Υ_B (see Fig. 4). Table 1 lists the best-fit values for these parameters and the difference in log-likelihood between the two models. For the SIS model, we find $\sigma_0 = 272_{-5}^{+19}$ km s $^{-1}$, corresponding to a 9% uncertainty in the mass. The fit of the best solution to the data is shown in Fig. 5. For the constant M/L model, we find $\Upsilon_B = 7.3 \pm 0.2$. This model fits the data far worse than does the best SIS model (6 σ significance), providing strong evidence for a dark matter halo in this galaxy.

The poor fit of the constant M/L model apparently stems from its inability to reproduce the constant $\hat{\sigma}_p(R)$ profile in the outer regions ($R \gtrsim R_{\text{eff}} \simeq 100''$) without also changing the shapes of the LOSVDs beyond the limits permitted by the data at $R \gtrsim 10''$ (see Fig. 5). To check this interpretation, we have tried models which lack some of these constraints (Table 1). The h_6 measurements seem to be critical constraints, since without them, the constant M/L model is ruled out at only 2 σ . In the absence of any higher-order LOSVD information (no h_4 or h_6), the constant M/L model cannot be ruled out — the nearly-constant $\hat{\sigma}_p(R)$ profile can be reproduced by extreme variations in the orbit anisotropy (*e.g.*, a DF which is very radial at small radii and very tangential at large radii). Even without the ST constraints on $\hat{\sigma}_p(R)$ ($R > 28''$), the (h_4, h_6) measurements rule out the constant M/L model at 3 σ , demonstrating the usefulness of these constraints. However, depending solely on (h_4, h_6) can be somewhat dangerous, since flattening of the galaxy along the line of sight can also distort the stellar LOSVDs (Magorrian 1999).

Note that the removal of the ST velocity measurements at large radii also reduces the inferred M/L to $\Upsilon_B = 6$, which is a better assessment of the mass of the stars alone, since they become more dominant at smaller radii. Similar values ($\Upsilon_B \sim 2\text{--}5$) have consistently been found by detailed dynamical studies of the central regions ($R \lesssim R_{\text{eff}}$) of other nearby early-type galaxies (*e.g.*, Rix *et al.* 1997; van der Marel *et al.* 1998; Kormendy *et al.* 1998; Gerhard *et al.* 1998; Statler, Dejonghe, & Smecker-Hane 1999; Emsellem *et al.* 1999; Matthias & Gerhard 1999; however, Saglia *et al.* 2000 found $\Upsilon_B \simeq 10$ for the cD galaxy NGC 1399).

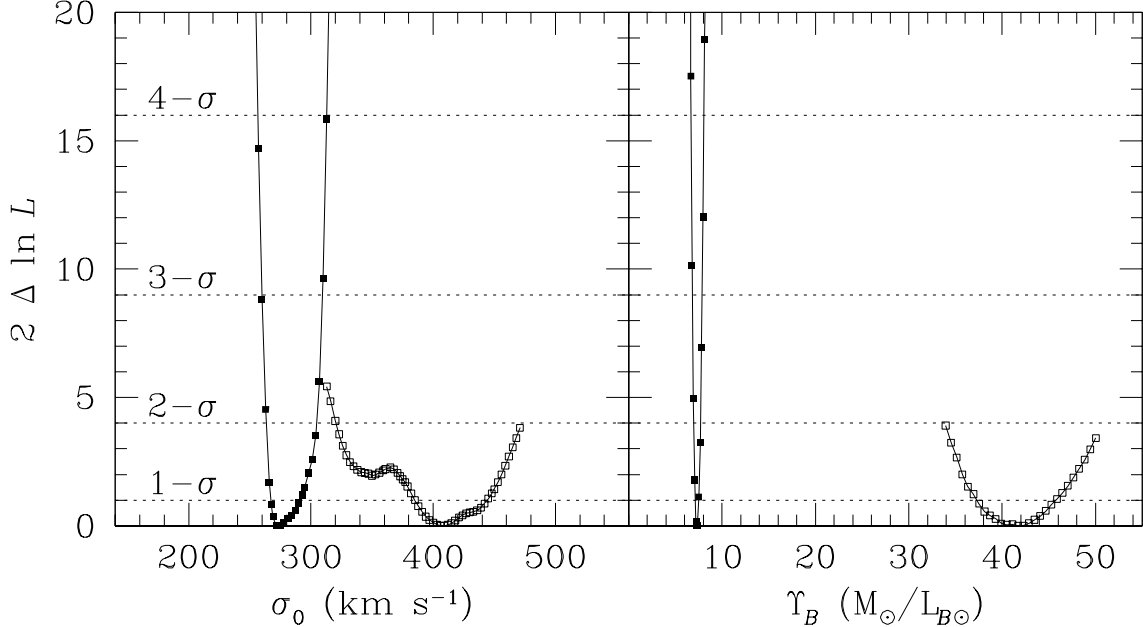


FIG. 4.— The log-likelihood of the best-fit singular isothermal model (*left panel*) and constant mass-to-light ratio model (*right panel*), as a function of the mass parameters σ_0 and Υ_B . The filled squares show the fit to the stellar data, and the open squares the fit to the globular cluster data.

Constraints	Singular Isothermal		Constant M/L	
	σ_0 (km s ⁻¹)	Υ_B ($M_\odot / L_{B\odot}$)	$\Delta \ln \mathcal{L}$	
Stars: I , $\hat{\sigma}_{\text{vdM}}$, $\hat{\sigma}_{\text{ST}}$, h_4 , h_6	272_{-5}^{+19}	7.3 ± 0.2	21.2 (6.2 σ)	
Stars: I , $\hat{\sigma}_{\text{vdM}}$, $\hat{\sigma}_{\text{ST}}$, h_4	275_{-9}^{+19}	$7.8_{-0.2}^{+0.3}$	3.7 (2.2 σ)	
Stars: I , $\hat{\sigma}_{\text{vdM}}$, $\hat{\sigma}_{\text{ST}}$	275_{-12}^{+24}	$8.1_{-0.7}^{+1.1}$	0.05 (0.7 σ)	
Stars: I , $\hat{\sigma}_{\text{vdM}}$, h_4 , h_6	254_{-18}^{+22}	$5.8_{-0.4}^{+0.3}$	7.1 (3.4 σ)	
Stars: I , $\hat{\sigma}_{\text{vdM}}$, h_4	284_{-51}^{+34}	$7.2_{-1.8}^{+0.7}$	1.2 (1.2 σ)	
Globular clusters	409_{-24}^{+36}	$41.7_{-4.8}^{+4.2}$	17.3 (5.5 σ)	

TABLE 1.— M87 model solutions, given different sets of observational constraints. The best-fit mass parameters (σ_0 and Υ_B) are given for the SIS and constant M/L models. The difference in log-likelihood between the two models is shown, along with the statistical significance at which the SIS model is preferred. The “Bayesian” probability for the SIS model is $(1 + e^{-\Delta \ln \mathcal{L}})^{-1} \simeq 1$, while that for the constant M/L model is $e^{-\Delta \ln \mathcal{L}}(1 + e^{-\Delta \ln \mathcal{L}})^{-1} \simeq e^{-\Delta \ln \mathcal{L}}$ for $\Delta \ln \mathcal{L} \gtrsim 2$.

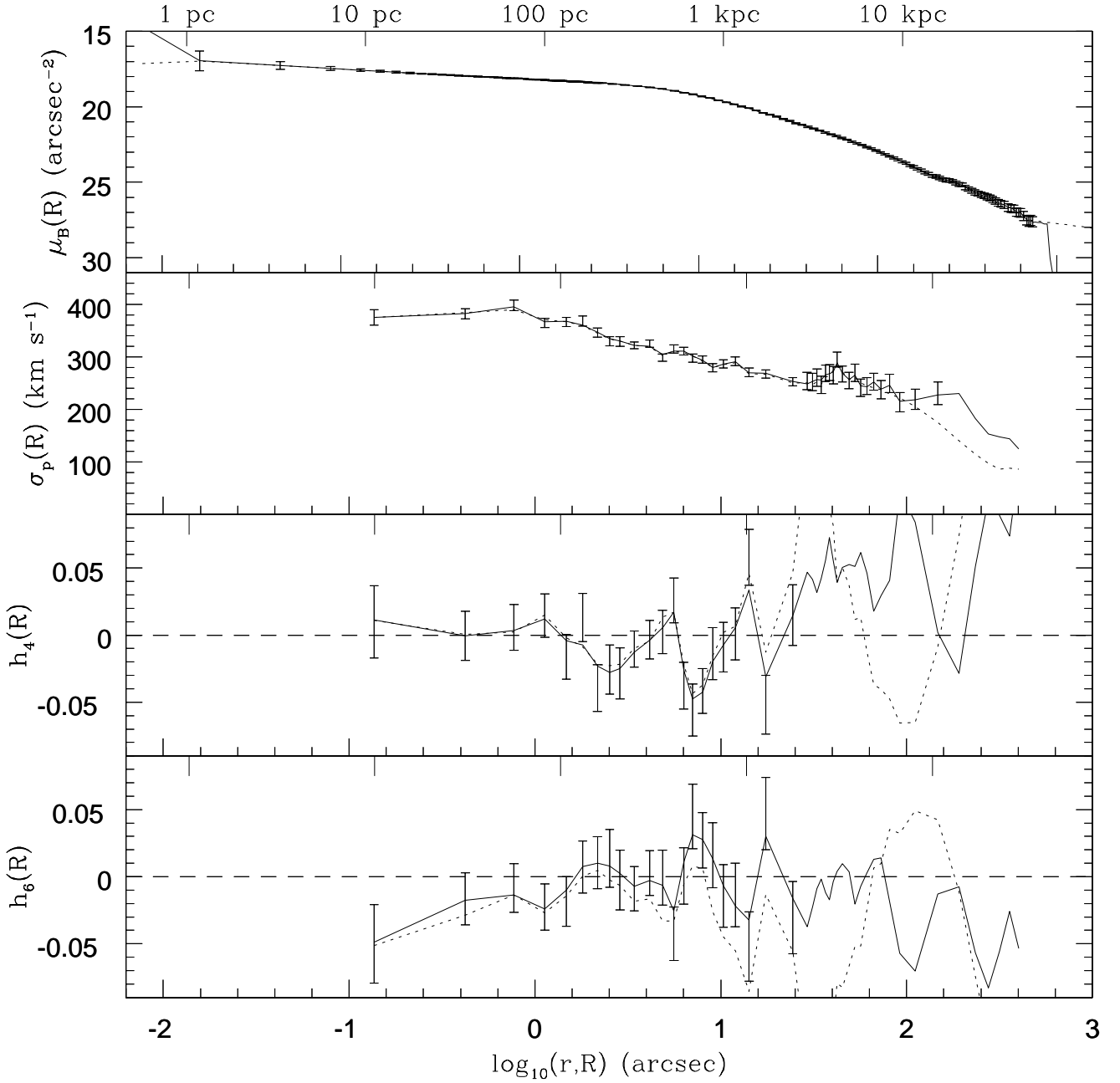


FIG. 5.— Fits to the M87 stellar data (error bars) for the best singular isothermal model ($\sigma_0 = 272$ km s $^{-1}$: solid lines) and for the best constant mass-to-light ratio model ($\Upsilon_B = 7.35$: dotted lines). The data are the radial profiles of the surface brightness, the velocity dispersion, and the fourth- and sixth-order Gauss-Hermite velocity moments (from top to bottom). Note that $R_{\text{eff}} \simeq 100''$.

Fig. 6 illustrates the orbital characteristics of the best-fit SIS solutions (with $\Delta\chi^2 \leq 1$), where the mean anisotropy is characterized by the parameter $\beta \equiv 1 - \langle v_\theta^2 \rangle / \langle v_r^2 \rangle$. These solutions suggest a somewhat radial DF in the region constrained by the kinematical data ($r \sim 0''.15\text{--}170''$). The dive toward tangential anisotropy near $r = 0''.7$ is due to the sharp turnover in $\hat{\sigma}_p(R)$ inside that radius. Real galaxies presumably have smooth $\beta(r)$ profiles, but with no smoothness imposed, our models are somewhat noisy because of the ill-conditioning of this inversion problem.

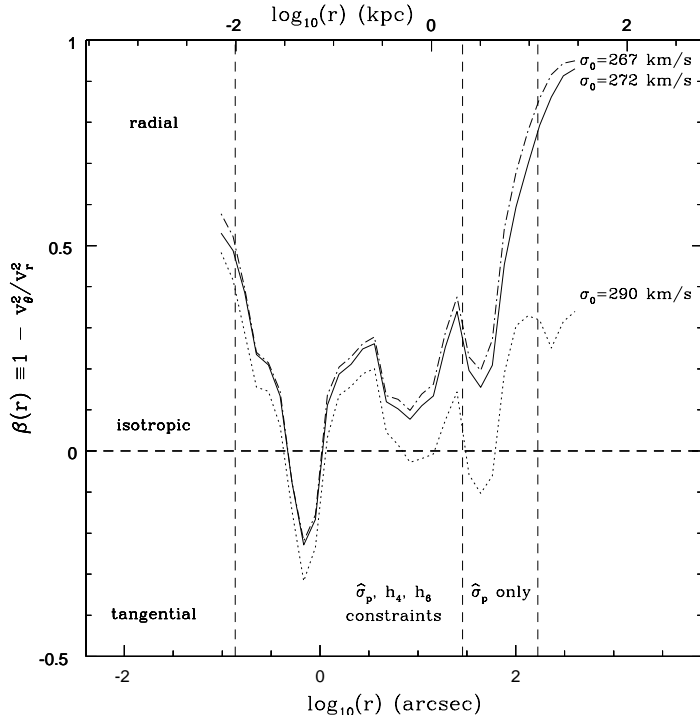


FIG. 6.— Stellar orbital anisotropy as a function of radius, for the singular isothermal potential. Solutions with three different mass normalizations are shown. The vertical dashed lines indicate the radial region constrained by the velocity data.

We fit the GC data to the same two mass models (see Fig. 4 and Table 1). For the SIS model, we find $\sigma_0 = 409^{+36}_{-24}$ km s $^{-1}$, corresponding to a 14% uncertainty in the mass. The fit of the best SIS solution to the data is shown in Figs. 7–9. Note especially in Fig. 8 that many of the higher-order features of the observed LOSVDs are reproduced by the model. For the constant M/L model, we find $\Upsilon_B = 42^{+4}_{-5}$. As with the stellar constraints, this model is significantly less probable than the SIS model (6 σ significance). Here, the constant M/L model cannot reproduce the radially-rising GC velocity dispersion profile (see Fig. 7). Also, $\Upsilon_B = 42$ is implausible for a standard stellar population, requiring an age $\gg 17$ Gyr and a metallicity [Fe/H] $\gg 0.50$ (Worthey 1994), so that even if mass traced light, the mass could not consist of a standard stellar population. Finally, note that $\Upsilon_B = 42^{+4}_{-5}$ is completely inconsistent with 7.3 ± 0.2 as obtained via the stellar dynamics, unless there is a drastic radial gradient in the stellar population. We thus conclude that the constant M/L model is definitively ruled out for M87.

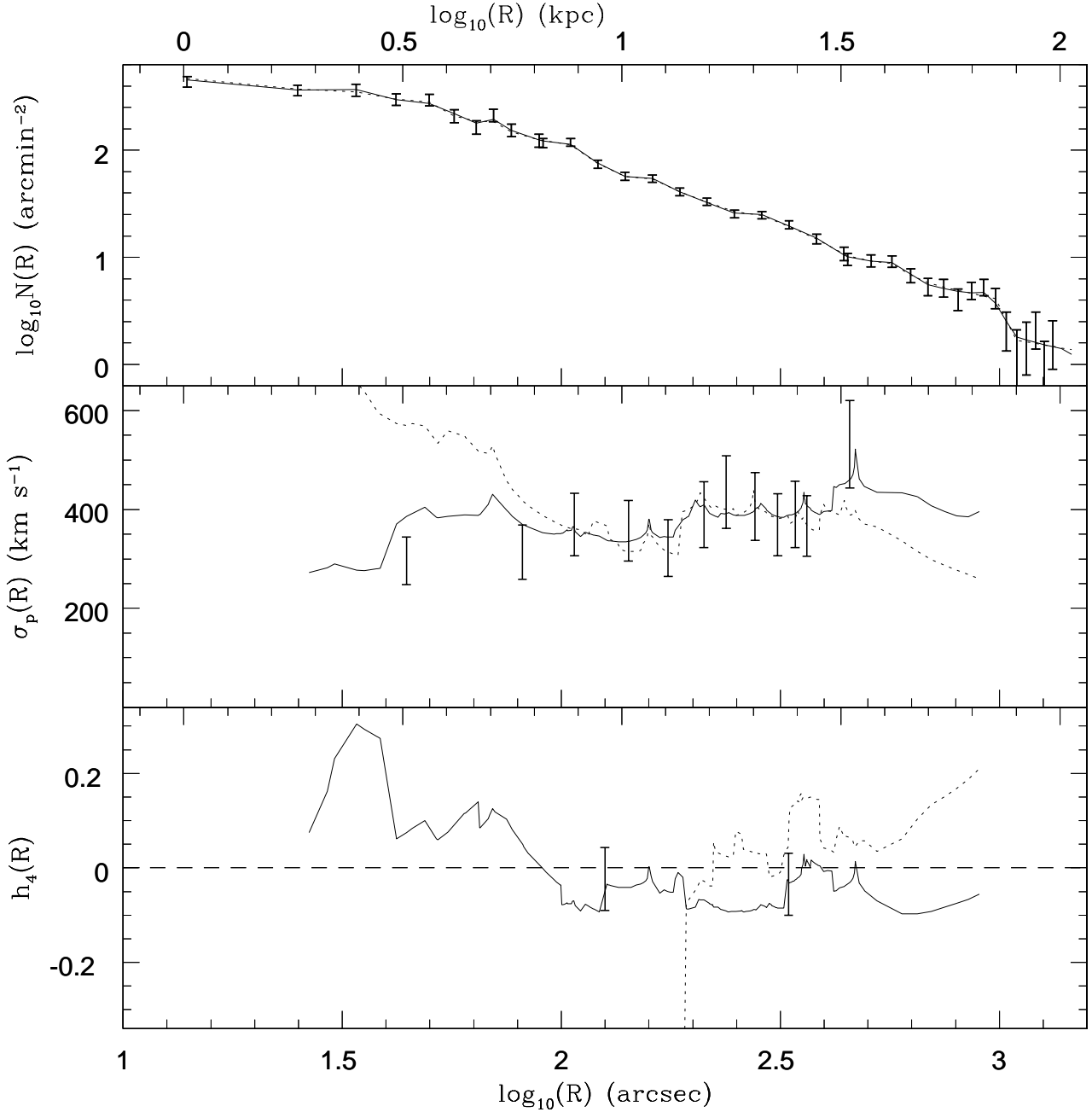


FIG. 7.—Fits to the M87 globular cluster data (error bars) for the best singular isothermal model ($\sigma_0 = 409$ km s $^{-1}$: solid lines) and the best constant mass-to-light ratio model ($\Upsilon_B = 41.7$: dotted lines). The data include the radial profiles of the surface density, the velocity dispersion, and the fourth-order Gauss-Hermite velocity moment (from top to bottom). Note that only the surface density is actually fit, while the other data are shown for comparative purposes only.

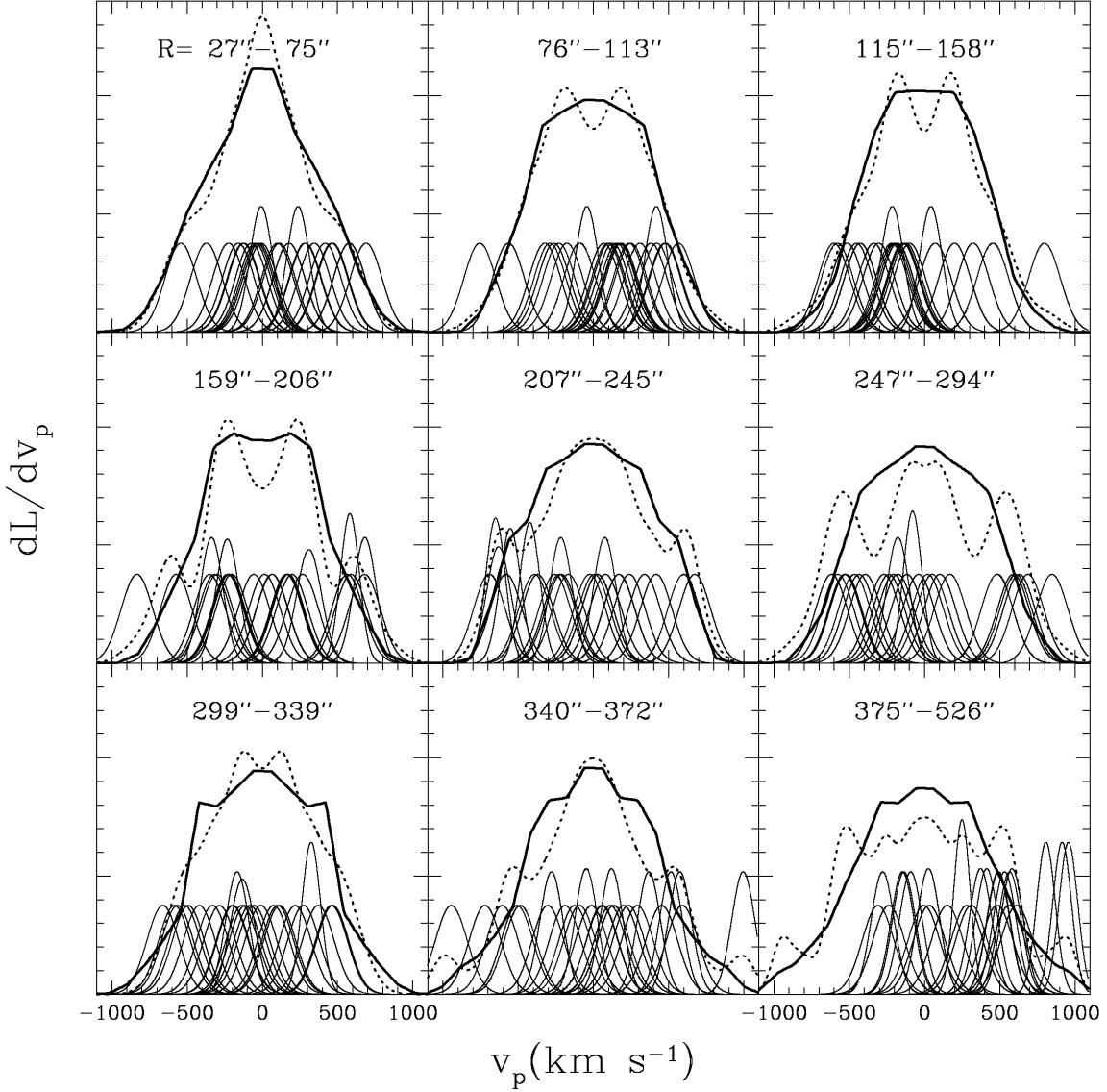


FIG. 8.— Line-of-sight velocity distributions for the M87 globular cluster system, in nine radial bins. The heavy solid lines show the LOSVDs of the best-fit solution ($\sigma_0 = 409 \text{ km s}^{-1}$), averaged in each bin. The light solid lines show the data (eleven points in each bin). The dotted lines show simulated LOSVDs derived from the superposition of the data in each bin, symmetrized about $v_p = 0$. Compare Fig. 3.

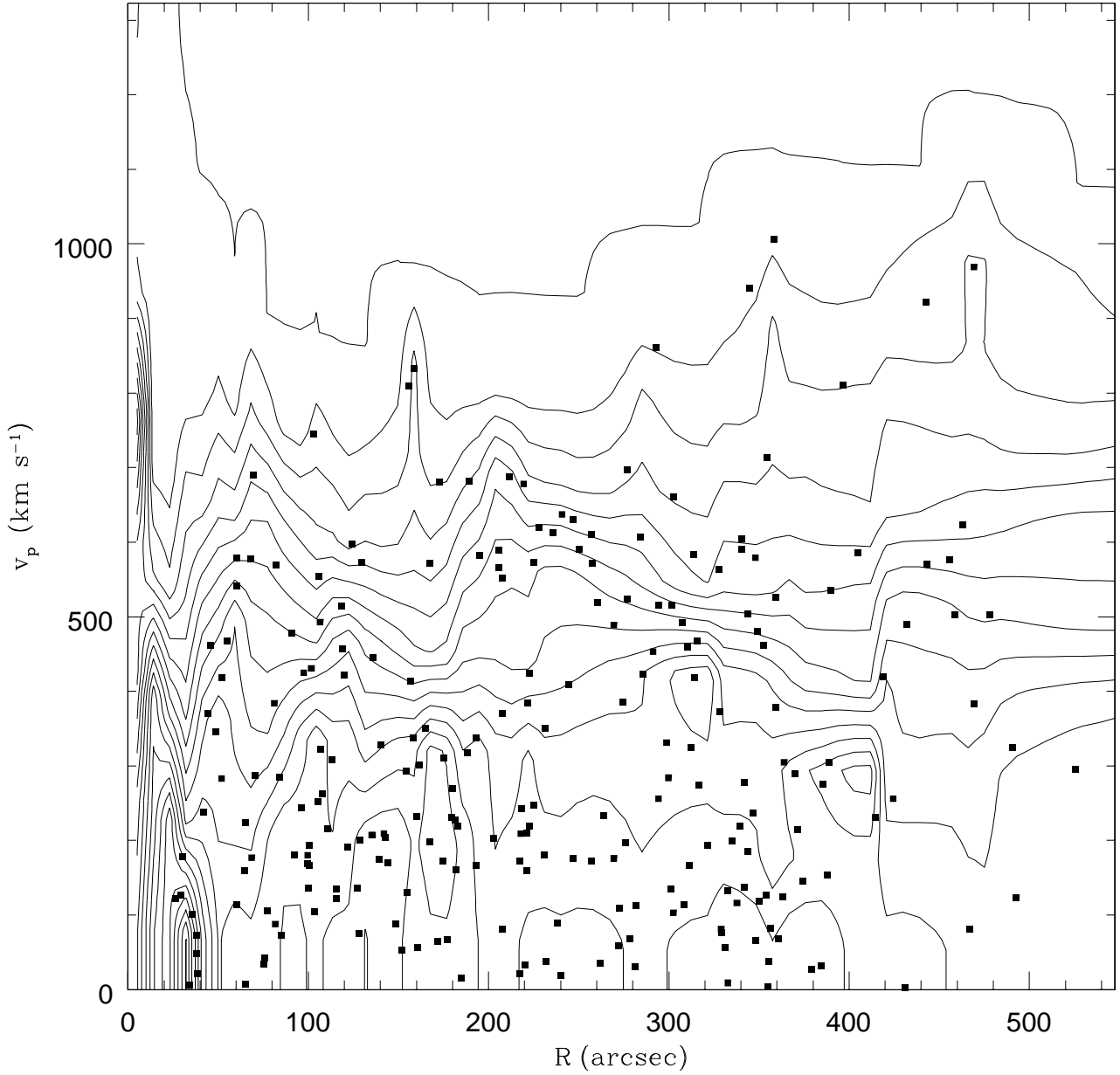


FIG. 9.— Contour plot of line-of-sight velocity distribution ($I^{-1} dI/dv_p$) for the best-fit globular cluster system model ($\sigma_0 = 409$ km s⁻¹), normalized by the surface brightness at each radius R . The last contour represents zero intensity. The data are shown as squares. Note that the model LOSVD is very peaked at small radii ($R < 50''$) and is very flat and even double-peaked elsewhere.

Fig. 10 shows the orbital characteristics of the best-fit SIS solution. There is a strong suggestion that the GC orbits are tangentially-biased over most of the radii covered by the velocity data, possibly becoming radial at smaller radii ($r \lesssim 30'' \simeq 2$ kpc). The tangential behavior is not surprising, given the flat and double-peaked LOSVDs seen in the data (see §2.4 and Figs. 8 and 9).

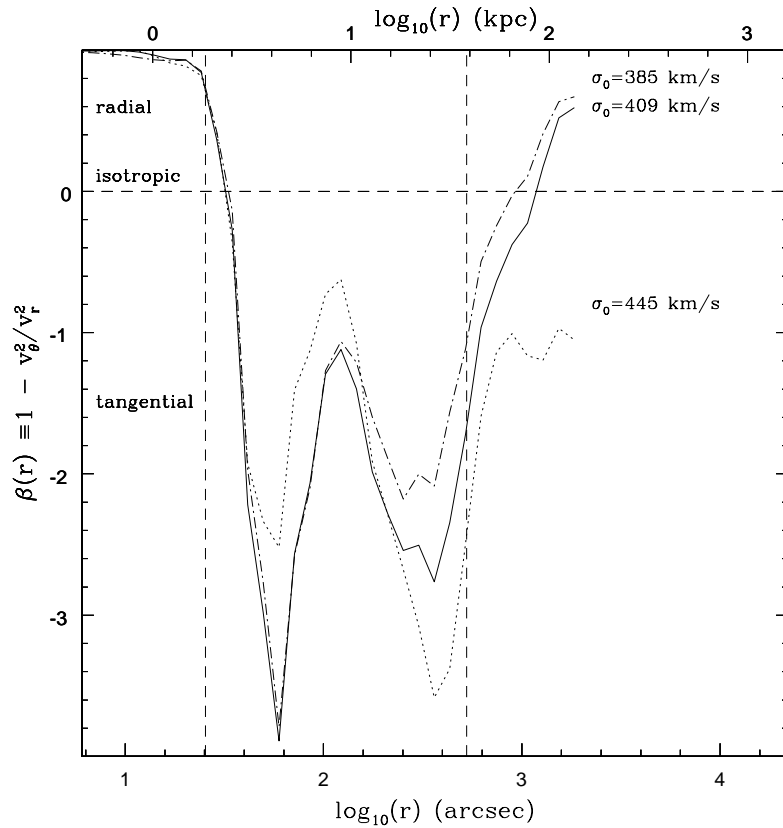


FIG. 10.— Velocity anisotropy of M87 globular cluster system models, as a function of radius, for singular isothermal potential. Three different solutions are shown. The vertical dashed lines indicate the radial region constrained by the velocity data.

5. CONCLUSIONS

We have developed a very general spherical orbit modeling method that makes use of all the information in a set of discrete velocity data, and have applied it to the galaxy M87 using all the available dynamical constraints (measurements of the spatial distribution and the kinematics of the stars and of the globular clusters). We find that taken on their own, the stellar and GC constraints each rule out a constant mass-to-light ratio model to a high level of significance. Assuming a singular isothermal mass profile, the stellar data determine the mass to 9%, while the GC data determine it to 14%.

In principle, we could combine the constraints from the stars and the GCs to put stronger limits on the mass of the galaxy. However, as with the constant M/L model, the SIS model masses implied by the two data sets are statistically inconsistent (99% confidence). The fact that σ_0 as derived from the GC data is *higher* than from the stellar data indicates that the density profile decreases more slowly with radius than $\rho \propto r^{-2}$. As shown in Fig. 11, the mass we derived from the GC data is consistent at large radii ($r \sim 500''$ – $4000''$) with the mass derived from the galaxy’s X-ray halo (Nulsen & Böhringer 1995), an analysis which also indicates a slow radial density decrease ($\rho \sim r^{-1.5}$). The natural interpretation of these facts is that the GCs reside in a transitional region where the dynamics of M87 begin to be dominated by the dark matter halo associated with the Virgo Cluster itself. In Fig. 11 we also compare our model results for the mass distribution with simpler estimates using the isotropic Jeans equations (see Sargent *et al.* 1978 equation 11 and compare CR Fig. 6). The profile $M(r)$ thus estimated from the stellar dynamics is consistent with our best-fit SIS stellar model, with $M(r)$ from the GC dynamics smoothly increasing to match our best-fit SIS GC model at large radii ($\sim 200''$).

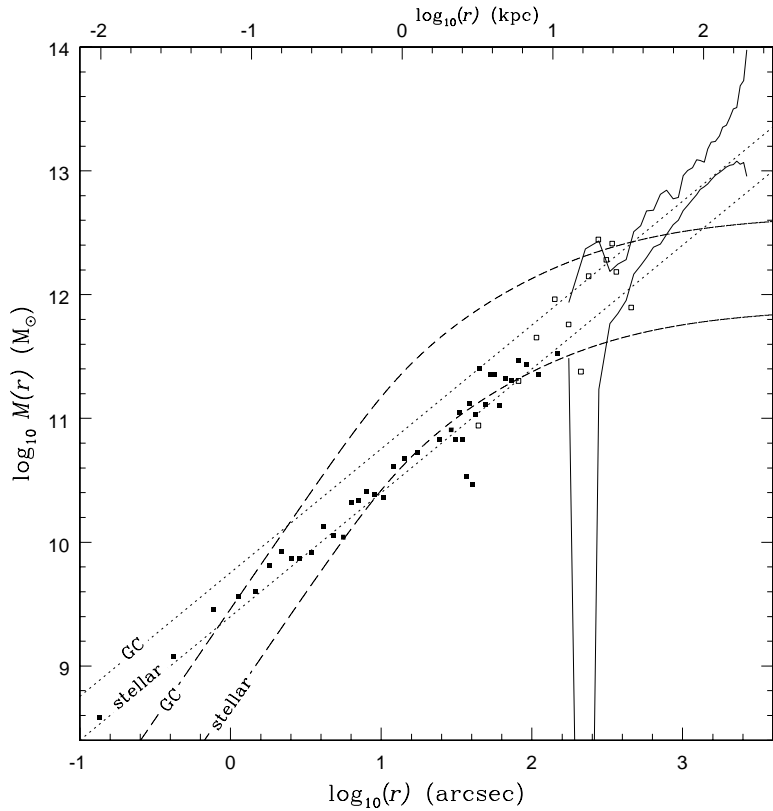


FIG. 11.— The radial mass profile of M87. The dotted lines show our best-fit SIS model to the stellar data ($\sigma_0 = 272 \text{ km s}^{-1}$) and to the globular cluster data ($\sigma_0 = 409 \text{ km s}^{-1}$). The dashed lines show our best-fit constant M/L models ($\Upsilon_B = 7.35$ and 41.7). The solid lines show the confidence limits from the X-ray analysis of Nulsen & Böhringer (1995). Also shown are estimates from the isotropic Jeans equations (see text) applied to the stars (*filled squares*) and the globular clusters (*open squares*).

While estimates using the Jeans equations may be qualitatively informative, our more sophisticated dynamical analysis is required to rigorously take into account the anisotropy uncertainties and to make full use of the data. This study has made use of only two simple mass models, but it would be straightforward to explore a wider range of models and determine the detailed mass profile $M(r)$ of M87, from its central parts well into the inner regions of the Virgo Cluster, using the joint constraints from the stars, the globular clusters, and the X-ray emission. An interesting starting point for these mass models would be the predictions from simulations of cosmologically-motivated structure formation (*e.g.*, Navarro, Frenk, & White 1996).

The same techniques should also be applied to other, non-cD giant elliptical galaxies in clusters (such as NGC 4472), as well as to galaxies in the field. The different formation histories of these galaxies (via mergers, accretion, etc.) may result in significantly different mass distributions and dynamics. Furthermore, the colors, abundances, and spatial distributions of the globular clusters in M87 and other galaxies indicate that they comprise two or more distinct populations (*e.g.*, Neilsen & Tsvetanov 1999; Gebhardt & Kissler-Patig 1999). It would be interesting to use our orbit modeling methods to look for any dynamical differences between these populations, which may shed light on their formation histories, for which several different scenarios have been proposed (*e.g.*, Ashman & Zepf 1992; Forbes, Brodie, & Grillmair 1997; Harris, Harris, & McLaughlin 1998; Côté, Marzke, & West 1998). The available set of kinematic tracers observed in the outer parts of early-type galaxies is now increasing rapidly, and we are hopeful that a much clearer picture of galaxy halos is forthcoming.

We thank John Blakeslee, Judy Cohen, Dan Fabricant, Marijn Franx, Lars Hernquist, and Konrad Kuijken for helpful comments; Ken Sembach for providing his data in tabular form; John Huchra, Roeland van der Marel, and Dean McLaughlin for both; Arunav Kundu for providing his paper in advance of publication, and his data in tabular form. C.S.K. is supported by the Smithsonian Astrophysical Observatory.

REFERENCES

Arnaboldi, M., Freeman, K. C., Gerhard, O., Matthias, M., Kudritzki, R. P., Méndez, R. H., Capaccioli, M., & Ford, H. 1998, *ApJ*, 507, 759

Ashman, K. M., & Zepf, S. E. 1992, *ApJ*, 384, 50

Binney, J., & Mamon, G. A. 1982, *MNRAS*, 200, 361

Binney, J., & Tremaine, S. 1987, *Galactic Dynamics* (Princeton: Princeton Univ. Press)

Boroson, T. A., Thompson, I. B., & Shectman, S. A. 1983, *AJ*, 88, 1707

Burstein, D., Davies, R. L., Dressler, A., Faber, S. M., Stone, R. P. S., Lynden-Bell, D., Terlevich, R. J., & Wegner, G. 1987, *ApJS*, 64, 601

Caon, N., Capaccioli, M., & Rampazzo, R. 1990, *A&AS*, 86, 429

Carollo, C. M., de Zeeuw, P. T., van der Marel, R. P., Danziger, I. J., & Qian, E. E. 1995, *ApJ*, 441, L25

Carter, D., & Dixon, K. L. 1978, *AJ*, 83, 574

Ciardullo, R., Jacoby, G. H., & Dejonghe, H. B. 1993, *ApJ*, 414, 454

Cohen, J. 1986, *AJ*, 92, 1039

Cohen, J. 2000, *AJ*, 119, 162

Cohen, J. G., & Ryzhov, A. 1997, *ApJ*, 486, 230 (CR)

Côté, P., Marzke, R. O., & West, M. J. 1998, *ApJ*, 501, 554

Davies, R. L., & Birkinshaw, M. 1988, *ApJS*, 68, 409

de Vaucouleurs, G., de Vaucouleurs, A., Corwin, H. G., Jr., Buta, R. J., Paturel, H. G., & Fouqué, P. 1991, 3rd Reference Catalogue of Bright Galaxies (New York: Springer-Verlag) (RC3)

de Vaucouleurs, G., & Nieto, J.-L. 1978, *ApJ*, 220, 449

Duncan, M. J., & Wheeler, J. C. 1980, *ApJ*, 237, L27

Emsellem, E., Dejonghe, H., & Bacon, R. 1999, *MNRAS*, 303, 495

Fabbiano, G. 1989, *ARA&A*, 27, 87

Federici, L., Bònoli, F., Ciotti, L., Fusi Pecci, F., Marano, B., Lipovetsky, V. A., Neizvestny, S. I., & Spassova, N. 1993, *A&A*, 274, 87

Forbes, D. A., Brodie, J. P., & Grillmair, C. J. 1997, *AJ*, 113, 1652

Gebhardt, F., & Fischer, P. 1995, *AJ*, 109, 209

Gebhardt, K., & Kissler-Patig, M. 1999, *AJ*, 118, 1526

Gebhardt, K., Richstone, D., *et al.* 2000, *AJ*, 119, 1157

Gerhard, O., Jeske, G., Saglia, R. P., & Bender, R. 1998, *MNRAS*, 295, 197

Grillmair, C. J., Freeman, K. C., Bicknell, G. V., Carter, D., Couch, W. J., Sommer-Larsen, J., & Taylor, K. 1994, *ApJ*, 422, L9

Haller, J. W., & Melia, F. 1996, *ApJ*, 464, 744

Harris, W. E. 1986, *AJ*, 91, 822

Harris, W. E., Harris, G. L. H., & McLaughlin, D. E. 1998, *AJ*, 115, 1801

Heisler, J., Tremaine, S., & Bahcall, J. N. 1985, *ApJ*, 298, 8

Hernquist, L. 1990, *ApJ*, 356, 359

Huchra, J., & Brodie, J. 1987, *AJ*, 93, 779

Hui, X., Ford, H. C., Freeman, K. C., & Dopita, M. A. 1995, *ApJ*, 449, 592

Jarvis, B. J., & Peletier, R. F. 1991, *A&A*, 247, 315

Kent, S. M. 1990, *MNRAS*, 247, 702

Kissler-Patig, M., & Gebhardt, K. 1998, *AJ*, 116, 2237

Kissler-Patig, M., Grillmair, C. J., Meylan, G., Brodie, J. P., Minniti, D., & Goudfrooij, P. 1999, *AJ*, 117, 1206

Kormendy, J., Bender, R., Evans, A. S., & Richstone, D. 1998, *AJ*, 115, 1823

Kundu, A., Whitmore, B. C., Sparks, W. B., Macchetto, F. D., Zepf, S. E., & Ashman, K. M. 1999, *ApJ*, 513, 733

Lauer, T. R., Faber, S. M., Lynds, C. R., *et al.* 1992, *AJ*, 103, 703

Magorrian, J. 1999, *MNRAS*, 302, 530

Mathieu, A., & Dejonghe, H. 1999, *MNRAS*, 303, 455

Matthias, M., & Gerhard, O. 1999, *MNRAS*, 310, 879

McLaughlin, D. E. 1999, *ApJ*, 512, L9

McLaughlin, D. E., Harris, W. E., & Hanes, D. A. 1993, *ApJ*, 409, L45

McLaughlin, D. E., Harris, W. E., & Hanes, D. A. 1994, *ApJ*, 422, 486

Merritt, D. 1993, *ApJ*, 413, 79

Merritt, D., Meylan, & Mayor, 1997, *AJ*, 114, 1074

Merritt, D., & Oh, S. P. 1997, *AJ*, 113, 1279

Merritt, D., & Saha, P. 1993, *ApJ*, 409, 75

Merritt, D., & Tremblay, B. 1993, *AJ*, 106, 2229

Mould, J. R., Oke, J. B., de Zeeuw, P. T., & Nemec, J. M. 1990, *AJ*, 99, 1823

Mould, J. R., Oke, J. B., & Nemec, J. M. 1987, *AJ*, 92, 53

Navarro, J. F., Frenk, C. S., & White, S. D. M. 1996, *ApJ*, 462, 563

Neilsen, E. H., Jr., & Tsvetanov, Z. I. 1999, *ApJ*, 515, L13

Newton, A. J., & Binney, J. 1984, *MNRAS*, 210, 711

Nulsen, P. E. J., & Böhringer, H. 1995, *MNRAS*, 274, 1093

Pierce, M. J., Welch, D. L., McClure, R. D., van den Bergh, S., Racine, R., & Stetson, P. B. 1994, *Nature*, 371, 385

Press, W. H., Teukolsky, S. A., Vetterling, W. T., & Flannery, B. P. 1992, *Numerical Recipes in C* (2d ed.; Cambridge: Cambridge Univ. Press)

Richstone, D. O., & Tremaine, S. 1984, *ApJ*, 286, 27

Richstone, D. O., & Tremaine, S. 1985, *ApJ*, 296, 370

Rix, H.-W., de Zeeuw, P. T., Cretton, N., van der Marel, R. P., & Carollo, C. M. 1997, *ApJ*, 488, 702

Romanowsky, A. J., & Kochanek, C. S. 1999, *ApJ*, 516, 18 (Paper I)

Saglia, R. P., Kronawitter, A., Gerhard, O., & Bender, R. 2000, *AJ*, 119, 153

Sargent, W. L. W., Young, P. J., Boksenberg, A., Shortridge, K., Lynds, C. R., & Hartwick, F. D. A. 1978, *ApJ*, 221, 731

Schombert, J. M. 1986, *ApJS*, 60, 603

Schwarzschild, M. 1979, *ApJ*, 232, 236

Sembach, K. R., & Tonry, J. L. 1996, *AJ*, 112, 797 (ST)

Sharples, R. M., Zepf, S. E., Bridges, T. J., Hanes, D. A., Carter, D., Ashman, K. M., & Geisler, D. 1998, *AJ*, 115, 2337

Statler, T. S., Dejonghe, H., & Smecker-Hane, T. 1999, *AJ*, 117, 126

Strom, S. E., Forte, J. C., Harris, W. E., Strom, K. M., Wells, D. C., & Smith, M. G. 1981, *ApJ*, 245, 416

Tenjes, P., Einasto, J., & Haud, U. 1991, *A&A*, 248, 395

Tonry, J. L. 1983, *ApJ*, 266, 58

Tremblay, B., Merritt, D., & Williams, T. B. 1995, *ApJ*, 443, L5

van der Marel, R. P. 1994, *MNRAS*, 270, 271 (vdM)

van der Marel, R. P., Cretton, N., de Zeeuw, P. T., & Rix, H.-W. 1998, *ApJ*, 493, 613

van der Marel, R. P., Evans, N. W., Rix, H.-W., White, S. D. M., & de Zeeuw, T. 1994, *MNRAS*, 271, 99

van der Marel, R. P., & Franx, M. 1993, *ApJ*, 407, 525

Winsall, M. L., & Freeman, K. C. 1993, *A&A*, 268, 443

Worthey, G. 1994, *ApJS*, 95, 107

Zeilinger, W. W. Møller, P., & Stiavelli, M. 1993, MNRAS, 261, 175